Experimental and Numerical Investigation of Rotor-Rotor Dynamic Interactions in a Tilting Multirotor System

Tanuj Sharma
University of Bristol
School of Civil, Aerospace and Design Engineering
Bristol, UK

Brano Titurus
University of Bristol
School of Civil, Aerospace and Design Engineering
Bristol, UK

Djamel Rezgui
University of Bristol
School of Civil, Aerospace and Design Engineering
Bristol, UK

ABSTRACT

This study aims to study rotor–rotor dynamic interactions in a tilting multirotor test rig through a combined experimental and numerical investigation. The rig was dynamically scaled to simulate the ordering and relative spacing of leading structural modes observed in NASA's X-57 DEP wing. An experimental modal analysis was performed under stationary and rotational conditions with shaker excitation, and the results were compared to a beam element based model simulated in MSC NASTRAN. The gyroscopic effects arising from propeller spin were introduced in the model using the Rotordynamics toolbox in MSC NASTRAN. The model was able to accurately represent the baseline structural dynamic response to within ±5% of experimental values and also captured key dynamic features such as mode frequency divergence, whirling and veering across the investigated rotor speed range. The dual rotor configuration, in contrast to the single rotor case, exhibited additional mode divergence, several distinct overlapping veering regions, and switching of mode shape properties. These results show that the coupled dual rotor configuration produces rich interaction-driven modal phenomena that transcend those encountered in isolated cases. The validated modelling method provides a basis for identifying such regimes and examining the effect of rotor spacing on the emergence and development of interaction-driven behaviour in multirotor systems.

NOTATION

*

Symbols

R Rotor radius (m)

Ω Rotor speed (rpm)

f Natural frequency (Hz)

ζ Modal damping ratio

E Young's Modulus (GPa)

G Modulus of Rigidity (GPa)

$I_{\mathbf{pxo}}, I_{\mathbf{pyo}}, I_{\mathbf{pzo}}$ Rotor polar moments of inertia (kg·m^2)

$L_{\mathbf{Beam}}$ Beam Length (m)

$L_{\mathbf{Arm}}$ Arm Length (m)

$m_{\mathbf{prop}}$ Mass of Propeller (kg)

$m_{\mathbf{hinge}}$ Mass of Tilting Hinge (kg)

W, H Width and height of the H-beam (m)

$t_{\mathbf{1}}, t_{\mathbf{2}}$ Flange and web thickness of H-beam (m)

$w_{\mathbf{arm}}, h_{\mathbf{arm}}$ Width and height of the hollow-arm (m)

$t_{\mathbf{arm}}$ Thickness of the hollow-arm (m)

*

Acronyms

DEP Distributed Electric Propulsion

DOF Degree of freedom

eVTOL Electric Vertical Take-Off and Landing

FE Finite Element

FRF Frequecny response Function

SQP Sequential Quadratic Programming

INTRODUCTION

Electrical vertical take-off and landing (eVTOL) vehicles have established a new frontier for sustainable and efficient urban mobility architectures based on Distributed Electric Propulsion (DEP) systems. These systems, embodied by vehicles such as Vertical Aerospace VX4, Joby S4, and Archer Midnight, employ multiple electrically driven rotors to enable both vertical lift-off and forward cruise, enabling rapid agility in manoeuvrability and minimising acoustic and emissions footprints. However, the multirotor design, especially when combined with an articulated tilting mechanism, poses a new set of dynamic issues. In particular, the simultaneous operation of multiple rotors creates complex rotor–roter interaction effects that strongly influence the vibrational behaviour, mode coupling, and stability of the vehicle (Refs. 1, 2). Understanding these interactions is important for predicting critical dynamic phenomena and designing robust DEP-based eVTOL vehicles.

Whirl flutter is an important aeroelastic instability for distributed electric propulsion (DEP) systems, whereby propellers are placed on flexible wings. The NASA X-57 program developed much of the framework to understand this instability. Multibody analysis with CAMRAD II, Dymore, and component mode synthesis was performed by Hoover et al. (2018) and Nelson et al. (2018) to investigate possible propeller placements and show that the final tip-mounted configuration was satisfactory and could avoid whirl flutter to up to 500 kts (Refs. 2, 3). This approach has been taken to further broaden and generalise the previous findings. Böhnisch and Braun (2022) presented a Doublet Lattice Method (DLM) aeroelastic model wherein the dominant instability can switch from whirl to wing flutter, dependent on rotor spanwise position and mount stiffness (Ref. 4). Böhnisch et al. (2023, 2024) also mapped the boundary regions between these regimes and provided preliminary design intent for flutter-free DEP wings (Refs. 5, 6).

Koch et al. (2024) implemented a frequency-domain transfer-matrix method and showed that moderate blade elasticity can stabilise backwards whirl, while large blade flexibility restored instability through coupling between the blades and airframe (Ref. 7). Koch et al. (2023) also showed that classical models, such as Houbolt-Reed, may poorly estimate instability threshold behaviours compared to mid-fidelity aerodynamic tools (Ref. 8). Despite this progress, previous studies have primarily focused on single rotor configurations. The dynamic implications of simultaneously spinning multiple rotors, such as gyroscopic coupling between rotors, structural interference of rotors, or modal coalescence when engaging multiple rotors, have largely been ignored, since almost all experimental studies have less than two active rotors. This is particularly relevant to DEP-based eVTOLs as spatially distributed rotors may operate at similar speeds and structurally interact with each other. Thus, the absence of studies focusing on rotor-rotor interaction provides the primary motivation for the current work.

Many recent studies have investigated the dynamic interactions of spinning rotors with their structures. Wu et al. (2023) designed and experimentally validated a beam–propeller rig to study moderate for single-rotor effects with time-varying conditions (Ref. 9). They were able to measure modal veering, frequency lock-in, and strong zero-order modulation as rotor speeds increased, and strong agreement was shown between the physical test and a non-linear time-periodic model. Wu et al. (2024) also looked at second blade-order count systematically and showed that two-blade rotors induce parametric instabilities due to periodic mass- and inertia-variation, whereas systems with three or more blades remain time-invariant (Ref. 10). These results highlight how gyroscopic and inertial couplings arising from a single rotor can drive intriguing structural dynamics, dependent on its configuration. Although these studies advanced the knowledge of rotor–structure interaction from an isolated system standpoint, none of these considered the dynamic interactions that arise due to two or more rotors operating simultaneously. In particular, the potential for cross-coupling between branches of whirling modes, their mutual gyroscopic interaction effects and coalescence with structural modes in close vicinity are yet to be studied. These are major limitations in the context of DEP-based multirotor platforms, where rotors placed on the common airframe are operating over a range of speeds. The current work will attempt to address this limitation by explicitly exploring how two rotors operating simultaneously interact through the structure.

A previous study introduced a dynamically scaled tilting multirotor test rig designed to replicate the modal behaviour of NASA's Maxwell X-57 eVTOL (Ref. 11). Through extensive experimental and numerical research, the work comprehensively characterises single-rotor-structure interactions, such as resonance interactions, forward and backwards whirling modes, and mode veering behaviours. Following those findings, the present research expands the modular rig to include two rotor assemblies: One rotor is placed at the spar tip, and the position of the second rotor changes to vary the rotor spacing. In the present study, rotor–rotor dynamic interactions are investigated systematically using a combined numerical and experimental approach. Experimental modal analysis is performed for each configuration of the test rig using an electromagnetic shaker. The modal analysis is compared against a 1D beam element model of the test rig made using MSC NASTRAN and PATRAN with gyroscopic effects introduced via the Rotordynamics toolbox.

The remainder of this paper is organised as follows: Section 2 introduces the dynamically scaled multirotor test rig, an outline of the numerical model in MSC NASTRAN and PATRAN, and experimental setup with shaker-based modal testing. Section 3 provides and reports experimental and numerical findings, e.g., baseline validation, rotor speed effects, and effects of rotor spacing on rotor–rotor interactions. Section 4 finally presents a summary of the key findings and provides a discussion on potential directions for future research.

METHODOLOGY

Overview of the Dynamically Scaled Multirotor Test Rig

Overview of the Multirotor Test Rig The experimental test rig employed in this study was developed to enable systematic investigation of tilting multirotor systems under controlled parametric variations. Drawing design inspiration from the distributed electric propulsion (DEP) configuration of the NASA Maxwell X-57, the rig incorporates a solid aluminium main spar with a machined H-shaped cross-section. This specific profile was selected to provide geometric tunability of the modal properties—particularly natural frequencies and mode spacing—during the initial design phase.

The main spar supports up to three rotor-arm assemblies. Each assembly consists of a brushless DC motor (MN2806-KV400) driving a three-bladed plastic propeller with a diameter of 10 inches and a pitch of 5 inches. The motors are mounted on rectangular hollow-section arms, which are clamped onto the beam. This clamping configuration enables flexible adjustment of rotor positions along the beam span. Each motor-arm assembly incorporates a mechanical tilting hinge, allowing manual variation of the rotor tilt angle to simulate DEP configurations with articulated thrust vectoring.

A low-fidelity finite element (FE) model based on Euler–Bernoulli beam theory was developed to guide the rig design. This FE model was coupled with an optimisation framework to iteratively refine the geometry such that the resulting modal characteristics—including target frequencies, spacing between modes, and effective mass distribution—exhibited dynamic similarity with the X-57 reference architecture. The resulting test platform thus serves as a versatile experimental setup for investigating modal characteristics (e.g., natural frequencies, damping, and mode shapes) and exploring complex rotor–structure interaction phenomena in multirotor systems. An overview of the complete test rig is provided in Figure 1.

Dynamically Scaling and Optimisation Methodology To ensure that the experimental rig replicates the key dynamic behaviour of a full-scale distributed propulsion system, a dynamic scaling methodology was implemented based on matching the modal characteristics of the NASA X-57 Maxwell configuration. The objective was to achieve dynamic similarity in terms of both the ordering and the frequency ratios of the primary structural modes—namely, the first out-of-plane, in-plane, second out-of-plane, and torsional modes.

An initial low-fidelity finite element model of the cantilevered beam was developed using Euler–Bernoulli beam theory, with rotor assemblies introduced as lumped masses and rigid connections. This model served as the foundation for a constrained non-linear optimisation process formulated in MATLAB using Sequential Quadratic Programming (SQP). The design variables comprised the geometric parameters of the H-shaped cross-section (height, width, flange and web thicknesses), which were tuned to minimise the squared error between the normalised natural frequencies of the test rig and the target spectrum. Additional constraints were imposed to preserve the sequence of mode types and to enforce practical manufacturability limits, while ensuring that the first four modes remained within the operational rotor speed range. The resulting geometry provided a rig that preserves the essential spectral features of the reference aircraft, enabling controlled exploration of rotor-structure and rotor-rotor interaction phenomena under realistic frequency spacing and mode coupling scenarios. Further details on the development, formulation, and validation of this dynamic scaling approach are reported in Sharma et al. (Ref. 8).

Table 1. Geometric and inertial properties used in the model.

Parameter	Value
W	3.55×10^{-2} m
H	1.25×10^{-2} m
t_1	4.00×10^{-3} m
t_2	1.35×10^{-2} m
m_e	1.00×10^{-1} kg·m
L_{beam}	8.25×10^{-1} m
I_{11}	4.46×10^{-9} m^4
I_{22}	4.62×10^{-8} m^4
g	9.81 m·s^{-2}
E	70.00 GPa
b_{arm}	2.50×10^{-2} m
h_{arm}	1.25×10^{-2} m
t_{arm}	1.50×10^{-3} m
m_{arm}	3.00×10^{-1} kg
L_{arm}	1.35×10^{-1} m
m_{prop}	$1.4.00 \times 10^{-2}$ kg
I_{pxo}	2.55×10^{-5} kg·m^2
I_{pyo}	1.25×10^{-5} kg·m^2
I_{pzo}	1.25×10^{-5} kg·m^2
N_b	3
m_{hinge}	1.40×10^{-2} kg

Optimisation Validation The final rig was built using the optimised beam geometry and component parameters obtained through the optimisation framework. The key geometric and mass properties of the beam, arms, and rotor assemblies obtained from optimisation have been summarised in Table 1. These correspond to the design solution targeted to match the reference dynamics of the NASA X-57.

To verify that the desired dynamic characteristics were achieved, experimental modal testing was carried out on the rig in the non-rotating configuration. Three rotor–arm assemblies were installed symmetrically along the span and fixed at 0° tilt. Modal identification was performed using an instrumented impact hammer, with responses measured via uniaxial accelerometers. The extracted modal properties, including natural frequencies and damping ratios, have been listed in Table 2 alongside their corresponding optimisation targets.

All four modes of interest were clearly identified. These included two bending modes (out-of-plane), one in-plane, and one torsional. Frequency agreement was strong: the largest deviation, just 3.06%, occurred in the second bending mode.

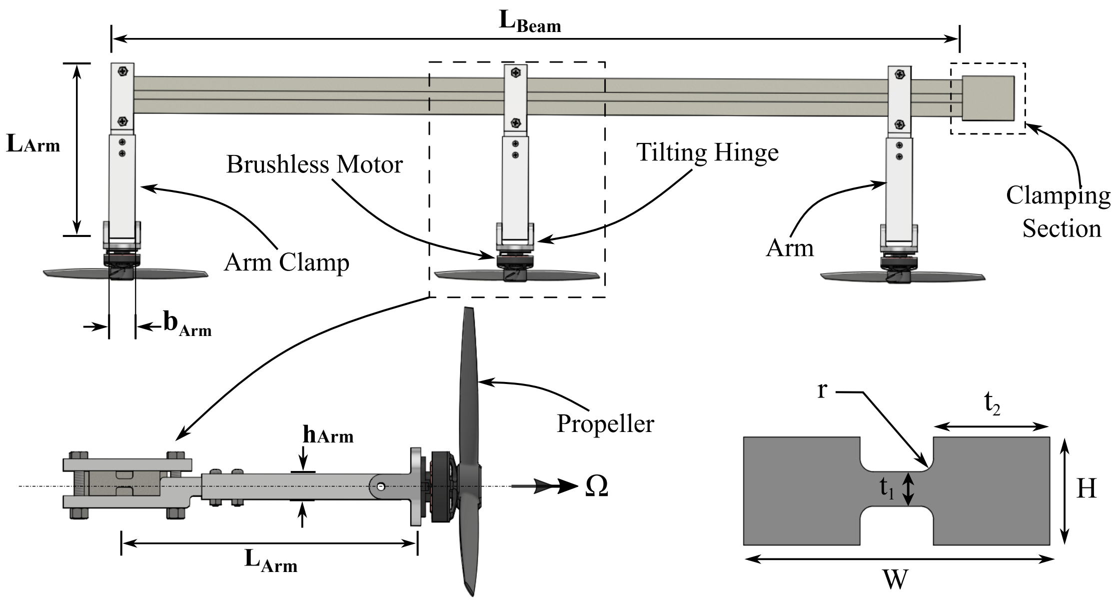

Figure 1. Overview of the Bristol Multirotor Test Rig Assembly.

Table 2. Natural frequencies of the multirotor test rig with three rotor and arm assemblies.

Mode	Optimisation [Hz]	Experiment [Hz]	Damping [%]
1st Bending	10.45	10.23 (2.13%)	0.60
1st In-Plane	32.11	31.66 (1.43%)	0.26
2nd Bending	62.88	64.07 (1.87%)	0.07
1st Torsion	78.58	76.21 (3.06%)	0.25

Damping values were consistently low, with the second bending mode having the lowest damping (0.07%). Importantly, the sequence of modal shapes matched the targeted order with no unexpected swapping of modes. This confirmed that the test retained the targeted modal properties and is suitable for investigating multirotor dynamic interactions under controlled experimental settings.

Numerical Model: 1D Beam Elements with Rotordynamics

To enable efficient yet dynamically representative simulations, a reduced-order finite element model was developed. The geometry definition and meshing were carried out in MSC PATRAN, while all dynamic simulations and post-processing were performed using MSC NASTRAN. The model was designed to capture the essential structural behaviour of the rig, with explicit inclusion of gyroscopic effects and rotor–bearing coupling. While originally built for correlation with experimental data, the model extends to exploratory simulations over a broader operational envelope.

Figure 2 illustrates the model architecture. A 1D beam-element representation was used throughout, accompanied by its 3D visualisation generated in PATRAN for clarity. The core structure comprises an H-section aluminium spar,

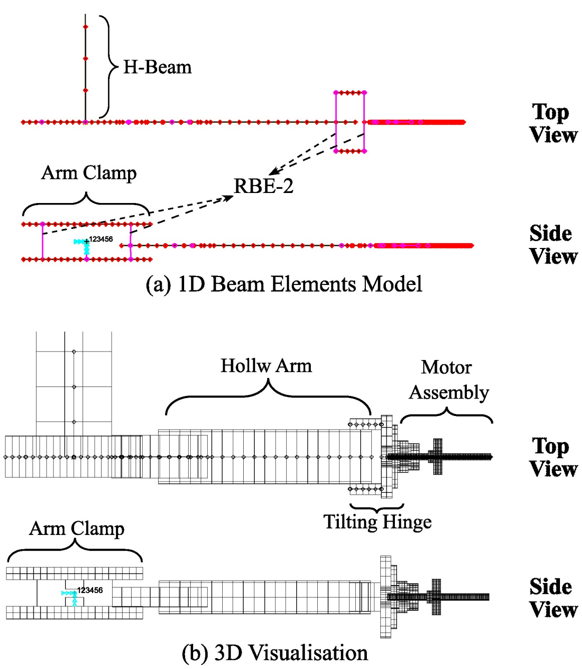

Figure 2. NASTRAN 1D Beam Element Model of Multirotor test Rig.

clamped rigidly at its root. A hollow rectangular arm is attached to this spar via discrete clamps and a tilting hinge sub-assembly. Each component was discretised using CBEAM elements. Rigid-body connections were enforced using RBE2 elements at bolted interfaces, such as the clamp-to-spar or hinge-to-arm junctions to replicate the high stiffness of physical connections. A fully fixed boundary condition was applied at the root node to replicate the cantilevered test setup.

The bearing interactions were modelled using a pair of CBUSH elements positioned at the bearing locations along

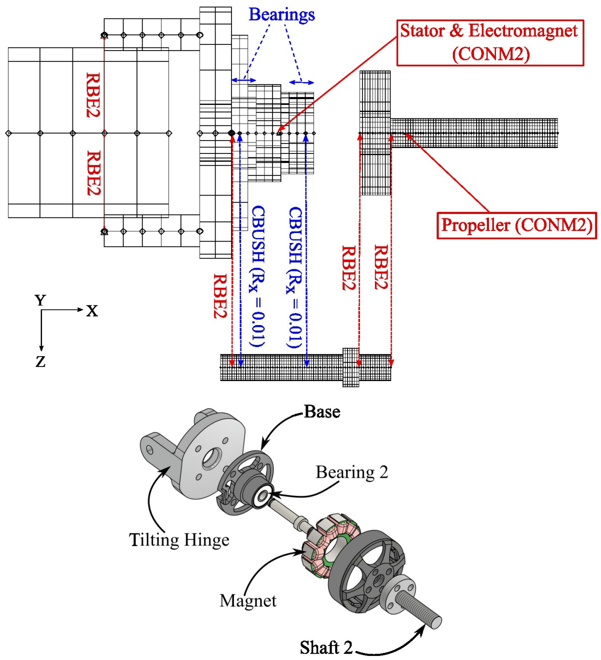

Figure 3. Detailed view of the motor assembly with all subcomponents

Shaft 1. These elements were aligned with the global x-axis, matching the shaft's axis of rotation. Stiffness values of 10^9 N/m and Nm/rad were assigned in all translational and rotational directions, except torsion about the x-axis (R_x), where a reduced stiffness (k_4 = 0.01 Nm/rad) was used to permit free rotation. This configuration constrains rigid-body motion while allowing axial spin, thereby emulating the rotor's ability to rotate freely within the bearing support structure.

The gyroscopic effects due to motor rotation were introduced using the Rotor Dynamics toolbox in MSC NASTRAN. This option adds gyroscopic terms in equations of motion, allowing one to simulate rotor–structure interaction under spin conditions accurately. For the 1D beam element model, the motor shaft, stator, magnet, and propeller nodes were regrouped into specific ROTORG entries. These were specified in the Rotor Node List field in such a way that gyroscopic terms were applied at the correct physical locations corresponding to the subcomponents which were rotating.

The model was solved using the SOL110 complex eigenvalue analysis, which accounts for gyroscopic coupling in rotating systems. A Campbell diagram was generated using CAMPBEL and DDVAL entries, which specified a rotor speed sweep from 0 to 4500 RPM in steps of 100 RPM. The solution provides a systematic investigation of dynamic properties dependent on the speed of the multirotor system.

Experimental Setup: Shaker-Based Modal Testing

A detailed view of the experimental setup is demonstrated in Figure 4. The test rig consists of an H-section aluminium beam clamped to a steel pod, which is bolted to a heavy metal block to create a rigid and vibration-isolated boundary condition. Two hollow rectangular aluminium arms are clamp-mounted along the span of the beam using arm clamps, and each arm carries a brushless electric motor (MN2806, KV400) mounted via a manually adjustable aluminium tilt adapter. Each motor drives three-bladed plastic propellers with a 12-inch diameter and 5-inch pitch (12×5). Motors are speed-controlled by a Teensy 4.1 microcontroller interfaced with independent 40A ESCs. was developed to interface with the Teensy and allows real-time control and adjustment of propeller speed during testing. This setup enables dynamic characterisation of the multirotor system at various steady-state operating conditions, to obtain frequency response functions (FRFs) and identify modal behaviour over an operating range of rotor speeds.

Dynamic excitation was offered by a permanent magnet electromagnetic shaker (LDS V201) that was securely fixed to a wooden pillar with a base clamped on an optical table to prevent recoil when actuated. The shaker was connected to the beam via a steel stinger and subsequently a PCB 208C04 piezoelectric force sensor. The force sensor was attached to the beam using an adhesive to ensure rigid contact and prevent dismount under high-frequency excitation. The shaker was driven with a power amplifier (gain = 4) having a National Instruments multifunction I/O module (NI 779205-01) connected to MATLAB. A sine-sweep excitation signal ranging from 0 to 400 Hz transmitted through the amplifier to the shaker, was used for exciting the test rig.

The system response was measured with five PCB 352A25 single-axis accelerometers, all mounted to the tip rotor assembly. Each of the sensors was mounted so as to measure motion along one degree of freedom: OP1 and OP2 measured out-of-plane bending; IP measured in-plane motion; and the remaining two measured torsion and pitch response. The position of each sensor was based on its sensitivity axis and on the local tip assembly geometry. The force sensor and the accelerometers were wired together using two input-only NI-9234 data acquisition modules. The DAQ modules were programmed with a MATLAB interface, where synchronous recording of all output and input channels was achievable.

The propeller speed was regulated by a Teensy 4.1 microcontroller connected with two 40A electronic speed controllers (ESCs) and potentiometers. A custom MATLAB-based application was developed to manage the entire test cycle: it allows the user to define a list of target rotor speed values, sets the motor speed accordingly, and synchronises the excitation and data acquisition process. For each rotor speed case, the software executes the sine sweep, collects all sensor and force data synchronously, and automatically saves the results. This system allowed efficient, repeatable testing over a wide range of operating conditions without human intervention.

RESULTS AND DISCUSSION

Baseline Modal Characterisation of Two-Rotor Configuration (0 RPM)

The initial validation study performed corresponds to a non-rotating baseline configuration of the test rig, which consists

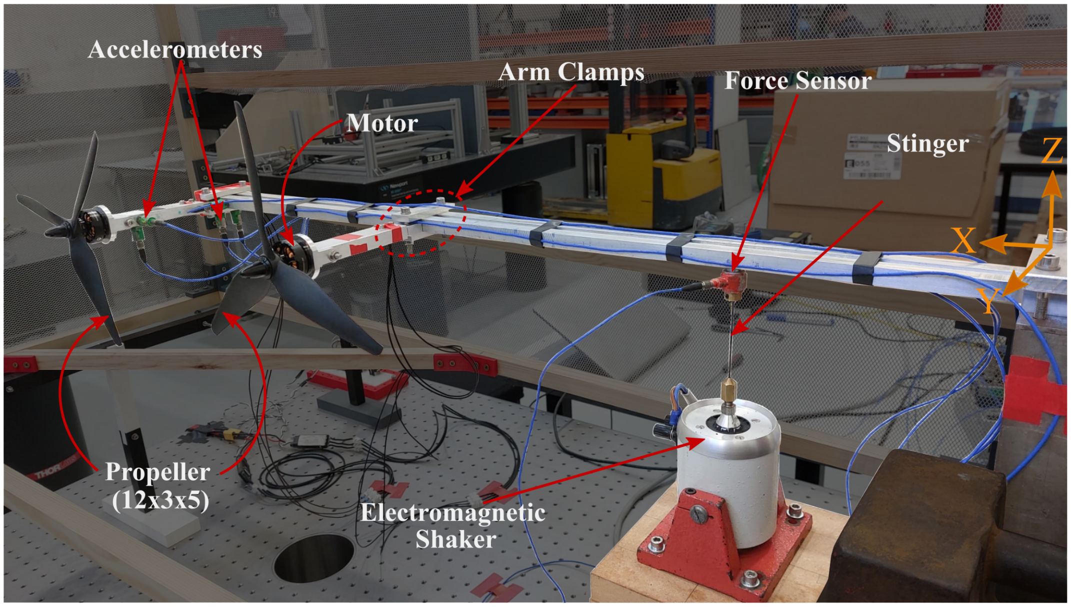

Figure 4. Shaker set-up

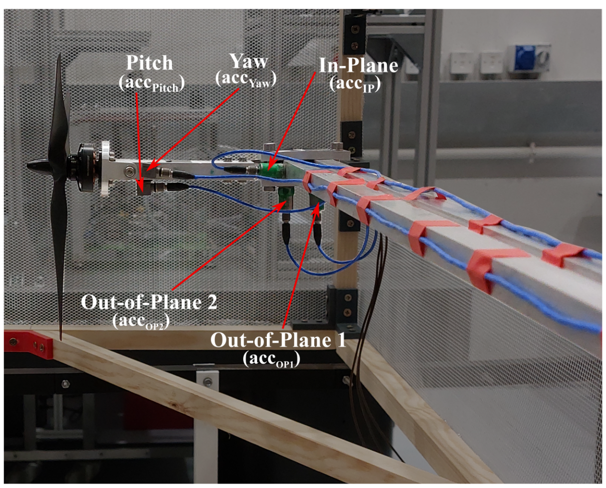

Figure 5. Accelerometer placement and orientation

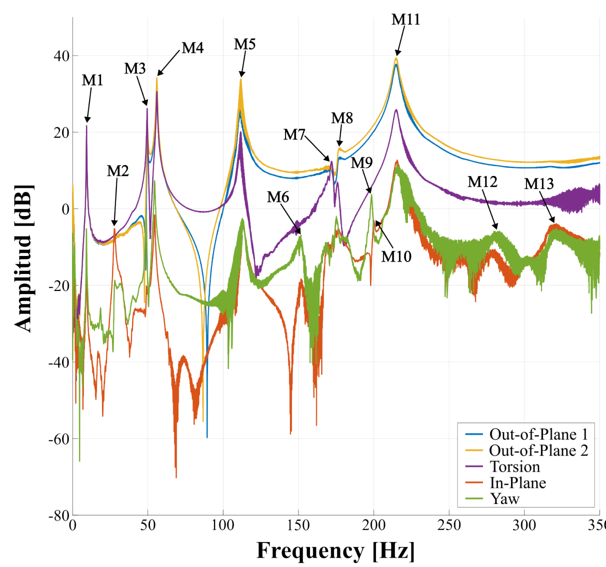

Figure 6. Experimentally obtained frequency response function plot at 0 RPM condition with inner rotor located at 40% beam length from the root.

of two rotor-arm assemblies attached to a main beam. The outer rotor was fixed at its tip, and the inner rotor was mounted at 40% of the total beam span, measured from the root. During this testing phase, the motors were not powered (0 RPM) to reveal the baseline structural dynamics behaviour, without influence from gyroscopic or aerodynamic contributions. This configuration was selected as the baseline for subsequent studies of rotor–rotor dynamic interactions. It allowed an explicit determination of the vibration modes in the absence of rotational excitation sources. The resulting modal properties are used as a reference point for the validation of the NASTRAN 1D beam model and for interpreting shifts due to rotor speed or spacing variations in subsequent sections.

To determine the baseline dynamic characteristics, experimental modal analysis was conducted. The excitation was applied in the out-of-plane (+z) direction by a modal hammer at 0.215 m from the root, and five uniaxial accelerometers were attached to capture the structural response of interest.

The Frequency Response Functions (FRFs) were computed in MATLAB using *modalfrf* function with H1 estimator, which takes the ratio of cross-power spectral density of output and input signals to the auto-power spectral density of input signal (Ref. 12). The FRF magnitudes are shown in Figure 6, where the horizontal axis represents the frequency and the vertical axis represents the acceleration-based FRF magnitude in dB. Resonant peaks related to structural modes can be clearly distinguished and are labelled M1 to M13 for traceability. Each mode was classified based on the sensor channel indicating the highest FRF magnitude. The natural frequencies and damping ratios were extracted from the FRF using MATLAB's modalfit function (Ref. 13). Estimation of the modal properties from the FRFs was done with the help of the *modalfit* function in MATLAB, using the LSRF fitting method. The estimated modal properties are listed in Table 3, along with the calculated natural frequencies obtained from the NASTRAN 1D beam model.

A numerical modal analysis in MSC NASTRAN was conducted using a 1D beam element model. The model consisted of CBEAM elements to simulate the main beam, while lumped masses were incorporated to simulate the inertial effects of the rotor-arm assemblies at the same positions as in the experimental setup. SOL 110 procedure was employed for eigenvalue extraction at rotor speed of 0 RPM so that the calculated natural frequencies represent the structural response without aerodynamic or gyroscopic effects in direct correspondence with the experimental case. The resulting natural frequencies from the NASTRAN model are presented alongside the experimentally identified frequencies and damping ratios in Table 3.

The comparison shown in Table 3 indicates a satisfactory correspondence between the experimental and computed natural frequencies. The discrepancies fall within ±5%, indicating that a simplified numerical representation adequately captured the dynamic behaviour of the multirotor configuration without spinning rotor effects. The largest error is observed in the second in-plane mode (M2), which has a deviation of 8.15%, or less than 1.5 Hz in absolute terms. The frequency deviations are expected due to the adopted modelling idealisations. Specifically, the use of discrete lumped masses to represent rotor-arm assemblies and the use of a simplified RBE2 representation of bolted interfaces can be seen as the primary source of the discrepancies.

The experimental damping ratios shown in Table 3 quantify the equivalent viscous energy dissipation characteristics of each mode and support the improved understanding of FRFs in Figure 6. Modes with low damping values, i.e., M3 (0.40%), M4 (0.53%), and M11 (0.98%), have narrow and tall peaks in the FRFs. They are expected to exhibit more distinct resonances and sustained vibration responses. Higher damping ratios in modes such as M2 (1.53%) and M13 (1.97%) have less prominent FRF peaks. This suggests higher energy dissipation and faster vibration attenuation.

Rotor Speed Effects on Rotor–Rotor Dynamic Interactions

In order to assess the effect rotor speed has on multirotor system dynamics, Campbell diagrams were created using both experimental and numerical methods. In the experimental cases, shaker-based modal tests were performed for a number of respective rotational speeds, from 0-4500 RPM, using discrete steps. At each rotor speed, the propeller speed remained constant while a sine-sweep excitation signal was imparted through an electromagnetic shaker. The output of the system response was measured with the help of five uniaxial accelerometers mounted on the tip rotor assembly. FRFs were calculated for each rotor speed case, while modal identification was conducted subsequently using the *modalfit* function in MATLAB (Ref. 12). Mode detection was enabled through the use of the LSRF fitting method to extract natural frequencies that were associated with distinct resonant peaks as the rotor speed changed.

The numerical Campbell diagrams were produced using the 1D beam element model previously described, using NASTRAN. The complex eigenvalue analysis was conducted for each configuration using the SOL 110 solution type with gyroscopic terms included. The rotor speed was varied across the same 0–4500 RPM range, and the CAMPBELL and DDVAL bulk data entries were used to evolve the asynchronous eigenvalue solution across this sweep. The resulting natural frequencies were extracted and overlaid onto the same plot as the experimental results for a direct visual comparison.

The Campbell diagrams obtained experimentally and numerically are presented in Figure 7, which has two subplots corresponding to two different test cases. Figure 7(a) shows the one-rotor spinning case where the RPM sweep was only applied to the tip rotor while the inner rotor was held stationary. On the other hand, Figure 7(b) illustrates the two-rotor spinning case, which had both rotors spun simultaneously at the same speed throughout the rotor speed sweep. In both figures, the horizontal axis represents rotor speeds (RPM) from 0-4500 RPM, and the vertical axis represents the natural frequency in Hz. The solid lines represent the predicted natural frequencies of the tracked structural modes from the NASTRAN model. Experimental modal frequencies, extracted at each rotor speed (RPM) point, are plotted using the dotted lines and distinct markers. Furthermore, the first harmonics of the rotation speed is also included as a dashed grey line in each subplot to help identify potential primary resonant regions. Each configuration demonstrated very good overall agreement between the experimental and numerical predictions. Hence, the numerical model not only matches the natural frequency values accurately at 0 RPM, but can also predict their variation with respect to rotor speed. In particular, this comparison demonstrates agreement in the important rotor dynamic characteristics including mode divergence and veering, as well as mode whirling characteristics.

Single Rotor Configuration – Tip Rotor Spins Only

Analysing the single-rotor configuration shown in Figure 7(a), where the tip rotor alone rotates, the Campbell diagram exhibits apparent divergent behaviour between Mode 9 and Mode 10, which begin in the frequency range of 192 -194 Hz, respectively, at 0 RPM. As the rotor speed increases, the frequency of Mode 9 decreases (backward whirl), whereas that of Mode 10 increases (forward whirl). At 1400 RPM, Mode 10 approaches Mode 11, whose curve remains nearly flat until 1300 RPM. In the range 1200–1600 RPM, both modes interact closely without intersection, marking a distinct modal veering region. Following this, Mode 10 frequency begins to plateau whilst Mode 11 adopts an upward trend, indicating a reversal in the sensitivity to the rotor speed.

To examine the veering behaviour further, Figure 8 shows the corresponding numerical Campbell diagram with the mode shapes from the NASTRAN model. This representation explicitly reveals the modal deformation patterns and their changes with rotor speed, especially in areas where there is strong modal coupling evident. At 0 RPM, Mode 10 features an in-plane dominated (IP2) structural pattern while Mode 11 displays an out-of-plane dominant pattern (OP3). In the veering region, at 1600 RPM, both modes display a very similar deformation pattern, essentially taking on the out-of-plane dominant shape resembling the deformation pattern of Mode 11 at 0 RPM. By reaching 3200 RPM, however, their mode shapes fully swap their characteristics, with Mode 10 now matching the original shape of Mode 11, and vice versa. This demonstrates a complete swap of the modal deflection pattern characteristics after the veering region has been passed.

The frequency of Mode 9 initially drops, but begins to plateau at about 1200 RPM as it couples with Mode 8. Although no distinct veering can be observed, the convergence of Mode 9 with Mode 8, and because Mode 8 is already closely spaced with Mode 7, produces a dense grouping of modes in the 175–185 Hz range. While the frequency variation of Mode 9 gradually flattens, Mode 6, which was initially insensitive to rotor speed changes, starts a progressive decrease in its frequency beyond 1000 RPM, manifesting the onset of backward whirl characteristics. This distinct change in the frequency trends suggests a redistribution of the gyroscopic effect among the modes, with the associated energy allocation varying as the rotor speed increases. This labelling of Mode 6 as a backward whirling mode is also confirmed by inspecting the mode shape plot of Figure 8, where the rotor-arm assembly is observed to experience precession motion in the direction opposite to the direction of the rotor spin.

Dual Configuration – Both Rotors Spin

Figure 7(a) presents the Campbell diagram for the configuration where both the inner and tip rotors were made to spin together across the rotor speed range. A more complex pattern of mode interaction is revealed in this case since there are two separate whirling rotor-arm assemblies. The mode tracking from the NASTRAN model shown in Figure 8 is used in conjunction with experimental modal data to investigate the nature of these interactions.

There are two distinct gyroscopic frequency divergence phenomena detected in this configuration, each being dominated by one rotor assembly. The first set of diverging modes is observed at lower frequencies between Modes 7 and 8, located in the frequency range of 169–178 Hz at 0 RPM. The second pair, represented by Modes 9 and 10, is found in the frequency range 192–197 Hz (as for the single-rotor spin case) and is linked to the forward and backward whirling branches of the tip rotor. These two pairs of modes render the modal density much greater and produce three distinct modal veering regions across the rotor speed range.

The first notable veering region occurs between Modes 8 and 9 at 300–800 RPM. In this region, the natural frequency of the forward whirling branch of the inner rotor (Mode 8) increases with rotor speed, and that of the backward whirling branch of the tip rotor (Mode 9) decreases with rotor speed. When these two modes interact, their frequency trajectories show a strong convergence up to 650 RPM. As the rotor speed increases beyond 650 RPM, the frequency trajectories diverge, and rotor speed trends are swapped — Mode 8 now begins to decrease with increasing rotor speed, and Mode 9 begins to increase with increasing rotor speed.

The second selected veering interaction occurs between Modes 6 and 7 in the 1000–1700 RPM range. Mode 6 is initially a yaw-dominated mode that is not sensitive to rotor speed, and Mode 7 is a torsion-dominated mode whose frequency decreases with rotor speed increase. As Mode 7 approaches Mode 6, a veering region is formed in a broad rotor

Table 3. Comparison of the natural frequencies between experiment and NASTRAN model of the Multirotor Test Rig at 0 RPM with inner rotor located at 40% beam length.

Mode	Type	f_{NASTRAN} [Hz]	$f_{\text{Experiment}}$ [Hz]	f_{Error} [%]	$\zeta_{\text{Experiment}}$ [%]
M1	Out-of-Plane 1	9.83	9.27	5.69	0.95
M2	In-Plane 2	30.78	28.27	8.15	1.53
M3	Torsion 1	50.84	49.52	2.59	0.40
M4	Out-of-Plane 2	58.52	55.93	4.52	0.53
M5	Out-of-Plane 3	108.21	111.45	2.99	0.88
M6	Yaw-1	158.53	152.26	3.95	0.94
M7	Torsion 2	169.65	172.48	-1.67	0.52
M8	Pitch 1	178.11	175.56	1.43	0.91
M9	Yaw 2	192.47	199.93	-3.87	0.67
M10	In-plane 2	193.76	201.32	-3.90	0.48
M11	Out-of-Plane 3	215.02	214.64	0.17	0.98
M12	Yaw 3	275.00	283.71	3.16	0.99
M13	In-Plane 3	306.35	320.63	-4.52	1.97

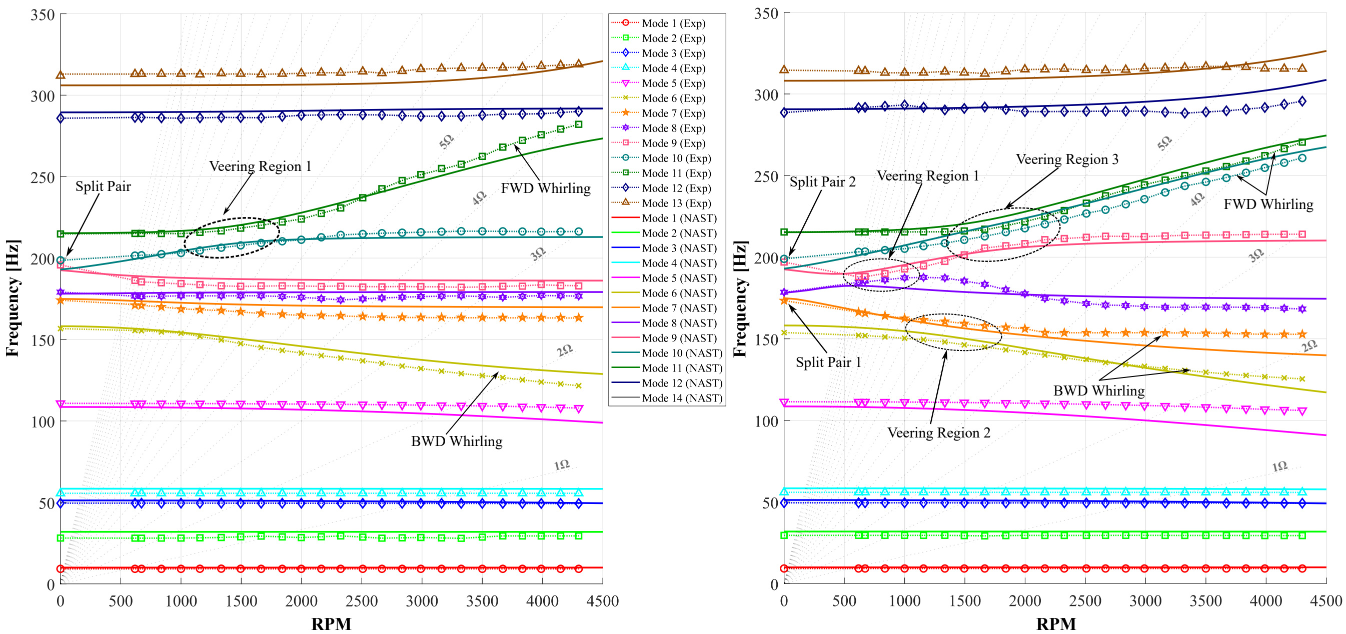

(a) Only Tip Rotor Spinning

(b) Both Rotors Spinning

Figure 7. Campbell diagram comparison for two configurations of the multirotor system with the inner rotor located at 40% of the beam span: (a) only the tip rotor is spinning while the inner rotor is non-rotating; (b) both the tip and inner rotors are spinning simultaneously.

speed range of 1000-1700 RPM. Beyond 1700 RPM, the frequency of Mode 6 starts to decline faster, while that of Mode 7 begins to plateau, which indicates a swap in the rotor speed sensitivity. Similarly, the modal deformation patterns between the two modes are swapped as they start to move beyond the veering region. At 0 RPM, Mode 6 is yaw-dominated, and Mode 7 is torsional-dominated. At 1600 RPM, both feature identical deflection patterns, with whirling of the rotor-arm assembly combined with yaw deformation. At 3200 RPM, the deformation patterns are reversed, where Mode 6 becomes torsion-dominant while Mode 7 becomes yaw-dominant. This reversal is represented in Figure 8 and can be observed on the beam, rotor-arm, and the sense of the gyroscopic motion response.

The third veering region is observed between Modes 10 and 11, beginning at approximately 1350 RPM. Mode 10 is initially the forward whirling branch of the tip rotor, whereas the frequency of Mode 11 is relatively insensitive to rotor speed changes. As the rotor speed approaches 1350 RPM, Mode 10 approaches Mode 11, and the two modes enter the coupling regime for the remainder of the sweep. Thus, it can be observed that Mode 11 adopts a trend of increasing frequency indicative of a forward whirling condition, similar to that of Mode 10. Furthermore, visually comparing the deformation patterns of Modes 10 and 11 at different rotor speeds shown in Figure 8, suggests the gyroscopically induced modal coupling, which influences the modal characteristics. At 0 RPM, the deformation pattern of Mode 10 is in-plane dominated (IP2), and that of Mode 11 is out-of-plane dominated.

At 1600 RPM, both modes feature nearly identical deformation patterns, with whirling of the tip rotor-arm assembly combined with out-of-plane deformation similar to that of mode 11 at 0 RPM. At 3200 RPM, whilst undergoing gradual transition, the deformation patterns are swapped, where Mode 10 becomes out-of-plane while Mode 11 becomes in-plane dominant with whirling of the tip rotor-arm assembly.

The overall presence of two spinning rotors generates a much richer modal landscape with an additional pair of strongly gyroscopically-sensitive modes and multiple overlapping veering regions. Each veering occurrence results in a corresponding change in the deformation pattern and whirling characteristics that clearly suggest that rotor–rotor interactions are not just additive but coupled. Furthermore, the model-experiment comparison suggests that these rotor–rotor interactions are consistently predicted by the model as confirmed by the trend in the Campbell diagrams in Figure 7.

Rotor Spacing Effects on Rotor–Rotor Dynamic Interactions

Figure 9 illustrates Campbell diagrams for the dual-rotor scenario, where both the tip and inner rotors were spun synchronously. The Campbell diagrams shown in the figure are obtained from the NASTRAN model. To isolate the impact of rotor spacing on the resulting modal interactions, different spanwise positions of the inner rotor were considered: 40%, 50%, and 60% of the beam length. The three subplots shown in Figure 9 correspond to each of these three spanwise locations of the inner rotor.

In all three cases, there are two pairs of modes demonstrating

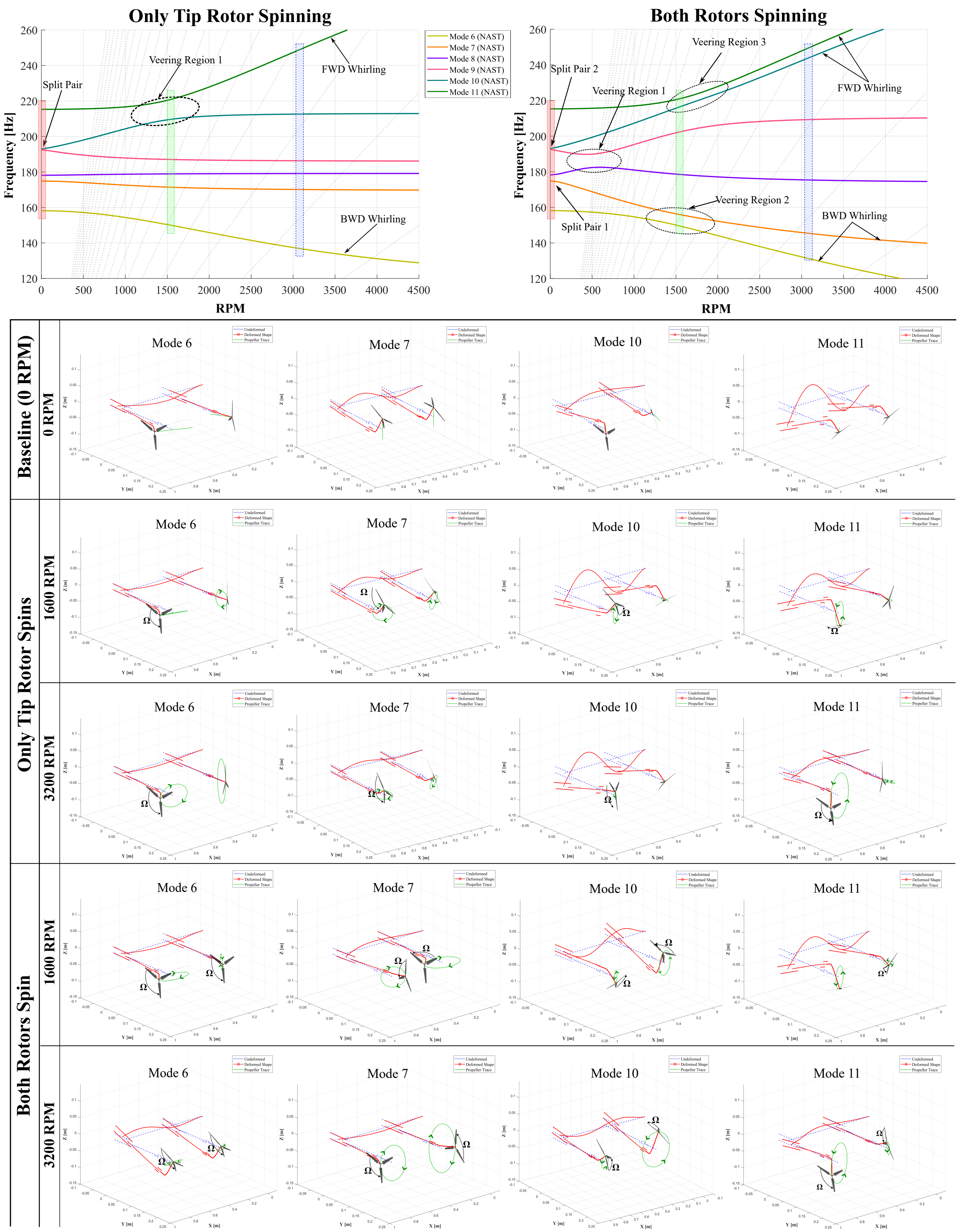

Figure 8. Campbell diagram comparison and mode shapes from NASTRAN model of two configurations of the multirotor system with the inner rotor located at 40% of the beam span: (a) only the tip rotor is spinning while the inner rotor remains stationary; (b) both the tip and inner rotors are spinning simultaneously.

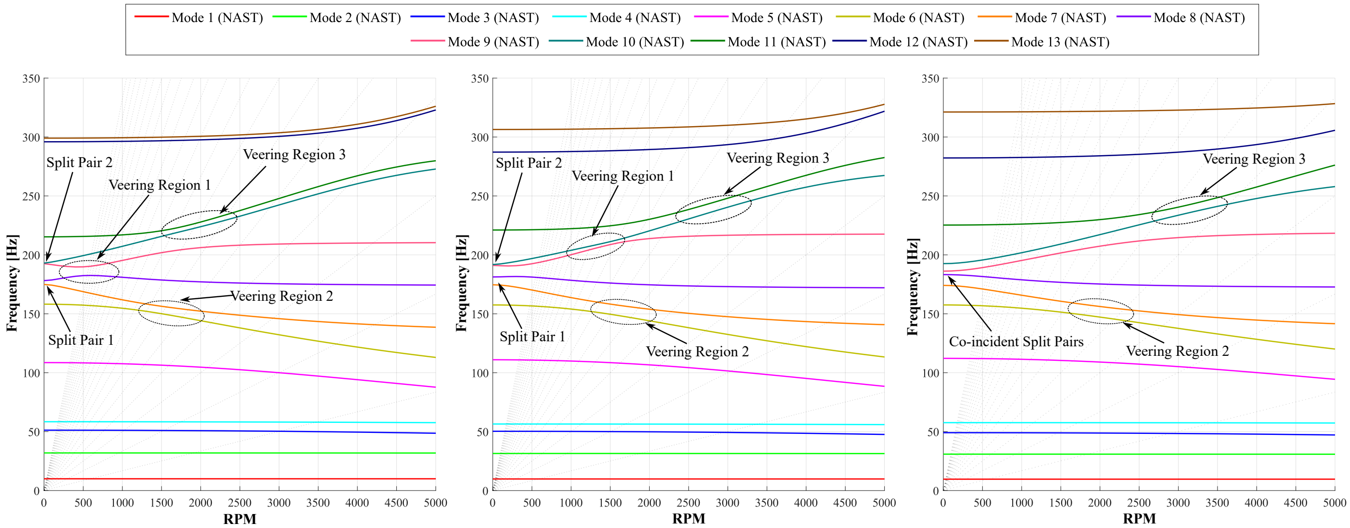

(a) Inner rotor at 40% length from from root

(b) Inner rotor at 50% length from from root

(c) Inner rotor at 60% length from from root

Figure 9. Campbell diagram comparison for three configurations with both rotors spinning. (a) Inner rotor located at 40% of the beam length from the root, (b) inner rotor at 50%, and (c) inner rotor at 60%.

a divergent divergence behaviour, each pair corresponding to one of the two rotors. At the 40% span station Figure 9(a) of the inner rotor, the two diverging pairs are clearly distinguishable at 0 RPM, with Mode 7 and Mode 8 (first pair) occurring at 174.88 Hz and 178.15 Hz, and Mode 9 and Mode 10 (second pair) emerging at 191.85 Hz and 192.98 Hz, respectively. The separation between the origin of these pairs results in a distinct veering region between the forward whirl branch of the first pair (Mode 8) and the backward whirl branch of the second pair (Mode 9), between 300 and 750 RPM.

When the inner rotor is moved closer to the tip (from 40%L to 60%L), the frequency of Mode 8 increases from 178.1 Hz to 183.3 Hz, and the frequency of Mode 9 slightly decreases from 192.9 Hz to 186.2 Hz. This brings the origins of the two divergent pairs closer together in frequency at 0 RPM. This eventually leads to a frequency gap between the origins of both diverging pairs becoming indiscernible in the 60%L case [Figure 9(c)], eliminating the first veering region.

The second veering region, which involves the interaction between Modes 6 and 7, also shifts as the inner rotor is relocated. In the 40%L configuration, this veering occurs between 1000 to 1700 RPM. As the inner rotor is moved closer to the tip, the region shifts progressively rightward, extending from 1300 to 2000 RPM for the 50%L case, and from 1500 to 2400 RPM for the 60%L configuration. This spatial progression is accompanied by a reduction in the slope of the frequency trajectories, suggesting a reduction of modal sensitivity to increasing the rotor speed.

The third veering region, between Modes 10 and 11, also shows a progressive shift. In the 40%L case, their modal coupling starts at approximately 1350 RPM and continues closely across the studied range. For 50%L, this zone is pushed to approximately 2200 RPM, and for 60%L to approximately 2500 RPM. Furthermore, for the 40%L and 50%L configurations, closely coupled frequency evolution persists through to 4500 RPM. However, in the 60%L configuration, the two branches begin to diverge once more after 4000 RPM, which indicates gradual modal decoupling with rising rotor speed.

Together, these results highlight how the spatial rotor–rotor localisation modulates the nature of modal interactions. As the inner rotor is moved closer to the tip, the system exhibits reduced separation between the diverging modes at the origin, resulting in obfuscation of certain modal interactions.

DISCUSSION

This study presented a combined experimental–numerical investigation of rotor–rotor dynamic interactions in a multirotor test rig. The rig was dynamically scaled to match the selected natural frequency ordering and modal spacing of NASA's X57 DEP wing. Specifically, the first out-of-plane, in-plane, second out-of-plane, and torsional modes were placed to form the same spectral sequence between the X57 wing and the rig. Validation was initially performed in the non-rotating state by performing experimental modal analysis using an electromagnetic shaker. A comparison was completed with a beam element model made in MSC PATRAN, which included gyroscopic terms to represent the rotors. The predicted natural frequencies were generally within ±5% of the measured ones, confirming satisfactory representation of the baseline dynamics. The rotational case validation was subsequently completed by direct comparison between the numerical and experimental Campbell diagrams throughout the 0-4500 RPM range. The model was shown to capture the prevailing dynamic features, such as whirling modal branches and veering regions with good qualitative agreement.

When only the tip rotor was operated, gyroscopic effects produced a clear and gradually increasing frequency separation between the closely spaced structural modes 9 (192 Hz) and 10 (195 Hz), forming forward and backward whirling modal branches. As speed increased, a particularly distinct veering region was formed between the out-of-plane (OP3) and in-plane (IP2) modes, leading to a complete swapping in the modal deformation characteristics. This veering behaviour was predicted by the numerical model and represented a manifestation of a strong rotor–structure interaction.

When both rotors were spun together, the dynamic response was considerably more complex. There were two distinct sets of divergent (divergent) modes, each corresponding to either rotor, which resulted in three notable veering regions. These regions were associated with inter-modal coupling and mode shape switching. The NASTRAN model correctly predicted all the major features during the 0–4500 RPM sweep, including the onset of whirling branches, mode interaction, and initiation and termination of veering behaviour between modes.

Further, by varying the spanwise position of the inner rotor from 0.4 L to 0.6 L, it was shown that rotor spacing directly influences the structure of the modal landscape. As the spacing was reduced, the separation between the origins of the two diverging pairs corresponding to each rotor at 0 RPM decreased, impacting the onset of the first veering region and associated modal coupling. These trends suggest that rotor spacing is an effective tuning parameter for managing adverse interactions in distributed propulsion systems.

CONCLUSION

This study demonstrates that rotor–rotor dynamic interactions in tilting multirotor systems give rise to complex modal interactional phenomena such as veering involving swapping of deformation patterns, increased modal density and emergence of highly gyroscopically-sensitive whirling modes associated with multiple concurrently spinning rotors. Such phenomena are not apparent from individual single-rotor analyses in isolation, and this study demonstrates the importance of modelling the entire multirotor assembly. This outcome has direct implications for the structural arrangement and control architecture of eVTOL aircraft with DEP configuration, where unanticipated alignment of the modal branches or transitions can exacerbate vibration levels, reduce control margins, or compromise structural integrity. By demonstrating how rotor speed and spatial arrangement influence the onset and evolution of these interactions, this work indicates a direction to prevent adverse dynamic coupling through early-stage design decisions. In this context, the validated numerical model provides an effective framework for predicting complex interactions in a multirotor system. In future efforts, this work will be further extended to include aerodynamic and tilting effects for full aeroelastic stability studies.

Author contact: Tanuj Sharma tanuj.sharma@bristol.ac.uk Brano Titurus Brano.Titurus@bristol.ac.uk Djamel Rezgui Djamel.Rezgui@bristol.ac.uk.

ACKNOWLEDGMENTS

The authors would like to thank the Engineering and Physical Sciences Research Council (EPSRC) for funding this research project under Grant No. EP/T517872/1.

REFERENCES

1. Kyle J Nelson and Jinwei Shen. Multi-propeller whirl flutter stability study using component mode synthesis element. In *AIAA SciTech 2023 Forum*, page 1509, 2023.

2. Jennifer Heeg, Bret K Stanford, Andrew Kreshock, Jinwei Shen, Christian B Hoover, and Roger Truax. Whirl flutter and the development of the nasa x-57 maxwell. In *International Forum on Aeroelasticity and Structural Dynamics (IFASD 2019)*, number NF1676L-31615, 2019.

3. Christian B Hoover, Jinwei Shen, Andrew R Kreshock, Bret Stanford, David J Piatak, and Jennifer Heeg. Whirl flutter stability and its influence on the design of the distributed electric propeller aircraft x-57. In *17th AIAA Aviation Technology, Integration, and Operations Conference*, page 3785, 2017.

4. Nils Böhnisch, Carsten Braun, Stephan Koschel, and Pier Marzocca. Whirl flutter for distributed propulsion systems on a flexible wing. In *AIAA Scitech 2022 Forum*, page 1755, 2022.

5. Nils Böhnisch, Carsten Braun, Vincenzo Muscarello, and Pier Marzocca. A sensitivity study on aeroelastic instabilities of slender wings with a large propeller. In *AIAA SCITECH 2023 Forum*, page 1893, 2023.

6. Nils Böhnisch, Carsten Braun, Vincenzo Muscarello, and Pier Marzocca. About the wing and whirl flutter of a slender wing–propeller system. *Journal of Aircraft*, 61(4):1117–1130, 2024.

7. Julia Noël, Christopher Koch, Bernd Stickan, H Bleecke, and Jürgen Arnold. Influence of blade elasticity and thrust on the whirl flutter stability of a propeller-driven aircraft. In *Proceedings of IFASD 2024: International Forum on Aeroelasticity and Structural Dynamics*. Hague The Netherlands, 2024.

8. Christopher Koch, Nils Böhnisch, Hendrik Verdonck, Oliver Hach, and Carsten Braun. Comparison of unsteady low-and mid-fidelity propeller aerodynamic methods for whirl flutter applications. *Applied Sciences*, 14(2):850, 2024.

9. Jun Wu, Djamel Rezgui, and Branislav Titurus. Model and experimental analysis of a rotor rig dynamics with time-varying characteristics. *Journal of Sound and Vibration*, 557:117683, 2023.

10. Jun Wu, Djamel Rezgui, and Branislav Titurus. Dynamics of nonlinear beam-propeller system with different numbers of blades. *Nonlinear Dynamics*, 112(2):833–863, 2024.

11. Tanuj Sharma, Djamel Rezgui, and Branislav Titurus. Experimental investigation into the dynamic characteristics of a tilting multirotor system. In *International Forum on Aeroelasticity and Structural Dynamics*, 2024.

12. MathWorks. Matlab modalfrf, 2024. Accessed: 2025-04-07.

13. MathWorks. Matlab modalfit, 2024. Accessed: 2025-05-03.

CLASSIFICATION & COPYRIGHT